Supplementary material - Design and fabrication of an electrostatic precipitator for infrared spectroscopy

Nikunj Dudani[1] and Satoshi Takahama[1]

[1]ENAC/IIE, Laboratory for Atmospheric Processes and Their Impacts (LAPI), École Polytechnique Fédérale de Lausanne (EPFL), 1015 Lausanne, Switzerland

Correspondence: Satoshi Takahama (satoshi.takahama@epfl.ch)

S1 Device details

The numerical simulations (Figure S1) in COMSOL Multiphysics was performed on a class of devices illustrated in the schematic of Figure 1a to obtain the steady state velocity and electrostatic field, to use for the transient particle tracing simulation and obtain the radial particle distribution on the crystal (Figure 1b). The device geometry from the simulations was replicated using 3D-printing a few parts (Figure S2) that allow removing and replacing the crystal from the device. The particle deposit was qualitatively analyzed using scanning electron microscopy (SEM) (Figure S3a, b, c) and optical microscopy (Figure S3d) to obtain the average radial scatter (Figure S3e).
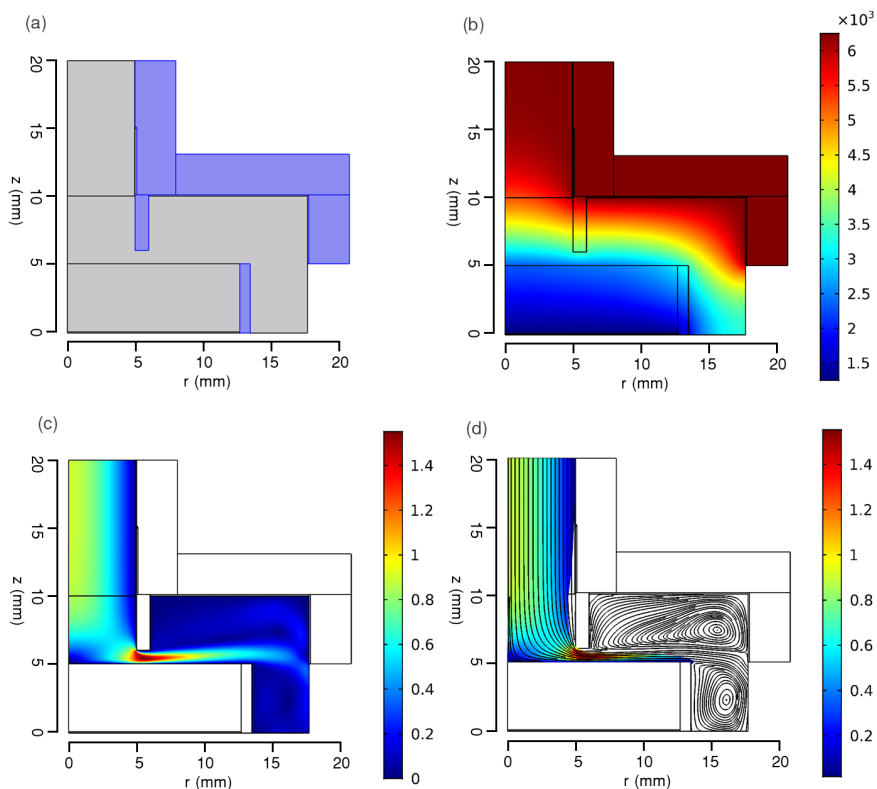
Figure S1. Numerical simulations of the ESP device for (a) the device schematic with the outer and inner body (ABS) highlighted, (b) steady state voltage field (V), (c) steady state velocity field (m/s), and (d) particle trajectories in the steady state field at the last time step.
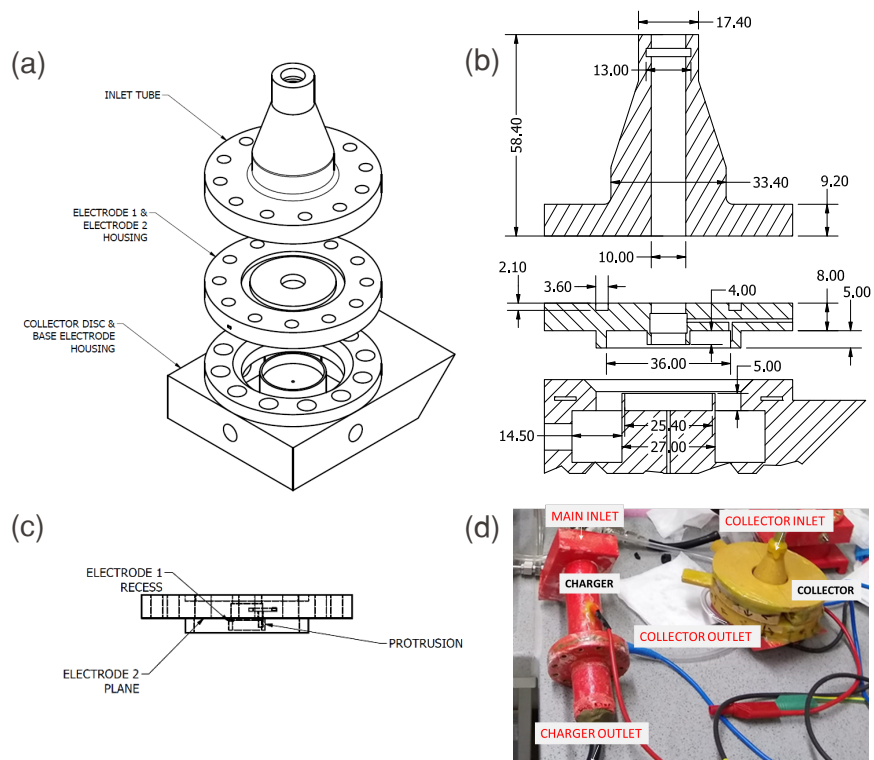
Figure S2. (a) Engineering drawing of the device assembly, (b) cross-section view with dimensions (in mm),(c) side view of the electrode housing part with the protrusion visible, and (d) fabricated and assembled device with the different parts labelled.
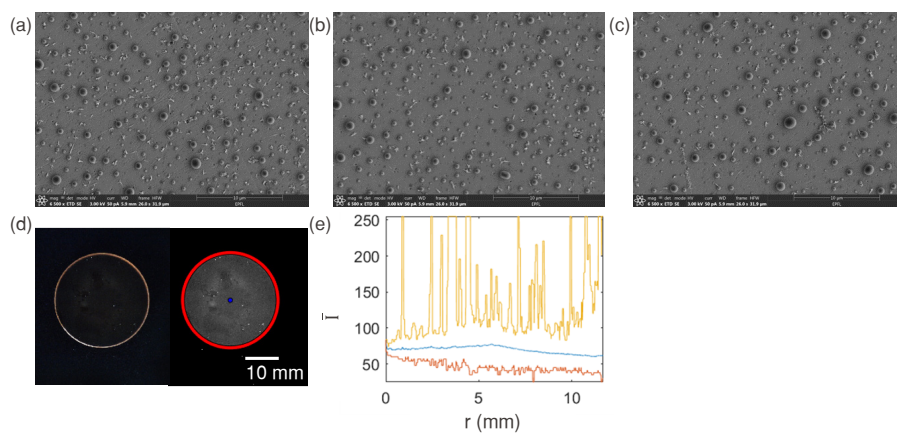
Figure S3. Scanning electron microscopy (SEM) images of the particle collection at a radius (a) 1 mm, (b) 6 mm, and (c) 9 mm away from the center. All scale bars are 10 μm long. (d) (Left) Top view image of particle loaded crystal and (right) the corresponding processed image (gray scale with center and circumference position). (e) Radial profile of average (blue), maximum (yellow) and minimum (red) gray scale scatter intensities (0 to 255) calculated from the processed image in panel d.

S2 Baseline correction

The spectra are baseline corrected using a smoothing spline fitting and subtraction (Kuzmiakova et al., 2016). The background points to which the smoothing spline is fitted can be identified using a number of methods (e.g., derivatives, mixture models, and asymmetric weights) (Liland et al., 2010; de Rooi and Eilers, 2012). In this work, background points were identified by setting limits on the moving mean and moving standard deviation on the slope of absorbance spectra. As the change in slope for sharp peaks or even broader peaks is higher than that for the baseline regions, using a combination of the change in the mean value and the deviation in slope allowed separating the baseline form the absorbance regions. For identifying the broad peaks (e.g. 2700 cm^{-1} - 3200 cm^{-1}), the moving mean of the absorbance itself is additionally used to separate it from the background.
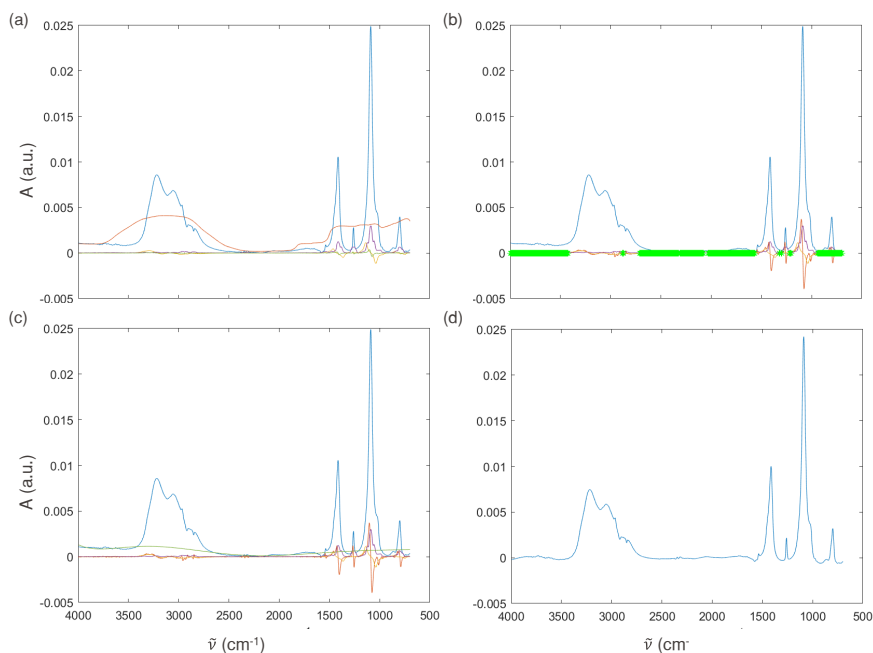
Figure S4. (a) Absorbance spectra (blue), moving mean of the absorbance spectra (red), slope of the absorbance spectra (orange), moving mean of the slope (green) and te moving standard deviation of the slope (purple). (b) Identified baseline points (green points). (c) A smoothed spline fitting the baseline points (green), and (d) the baseline corrected spectra.

S3   Quantitative analysis

The ratio of the reference volume absorption coefficient ($\alpha_{v,ref}$) to the linear absorption coefficient (α_{ref}) for ammonium sulfate calculated using n and k (Earle et al., 2006) shows the expected values of absorption coefficient in a heterogeneous medium against homogeneous (Figure S5a). Overall, the ratio is smaller than 1 for most wavenumbers and is rapidly changing around the peaks, which can result in shift in peak positions and also higher α for the heterogeneous medium case. When peak values at their respective maxima (for $\alpha_{v,ref}$ and α_{ref}) are compared, they are closer than these ratios at a given wavenumber indicate (Figure 5b and S6).

Polydimethylsiloxan (PDMS) contamination from sealing grease has absorption peaks for $Si\text{-}CH_3$ (800 cm^{-1} and 1260 cm^{-1}) and Si-O-Si (1130 - 1100 cm^{-1}). When the imaginary refractive index profile of PDMS (Myers et al., 2001) (congruent with absorbance for a homogeneous case) is scaled by the peak at 800 cm^{-1} and subtracted from the α_{10} profile for each experiment, the aforementioned peaks are no longer evident (including the shoulder of some peaks at 1110 cm^{-1}) (Figure S5b). Removing PDMS profile also lowers the height of the peak near 1110 cm^{-1} for SO_4. The corresponding response of IR against mass loading (Figure S6b) does not vary much from the response without the correction (Figure 5b) - R^2 remains the same and the slope decreases (to being 18% higher from the reference instead of 20% previously).

IR response against particle loading that does not use the image analysis of the optical microscopy images, rather uses a fixed density scaling factor $\phi_R(r_b) = 1$ (Figure S6a). The overall effect is that the points move in the abscissa when compared to Figure 5b.
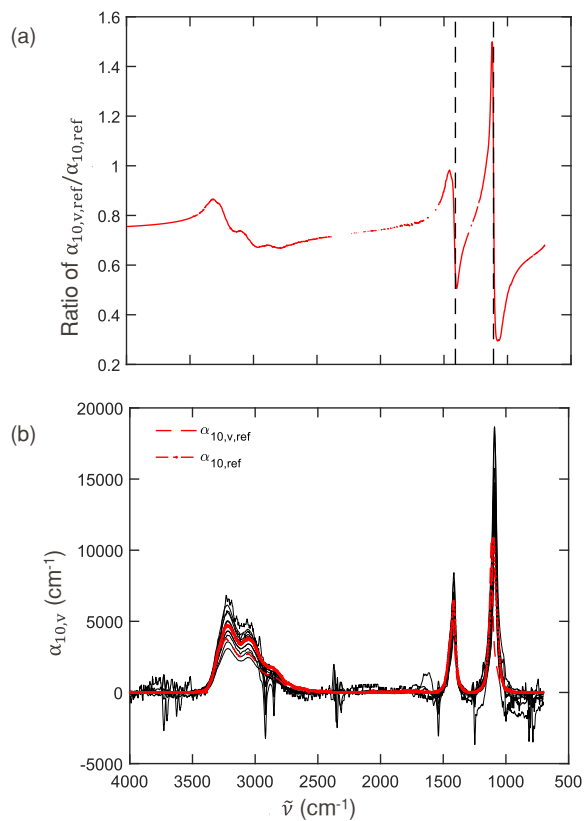
Figure S5. (a) Ratio of the reference volume absorption coefficient ($\alpha_{v,ref}$) to the linear absorption coefficient (α_{ref}) for ammonium sulfate calculated using n and k (Earle et al., 2006). (b) Comparison of modified volume absorption coefficient (α_v) adjusted by removing PDMS imaginary refractive index profile (Myers et al., 2001) (scaled by the peak at 800 cm^{-1}) from the calculated from the experiments as shown in Figure 5a.
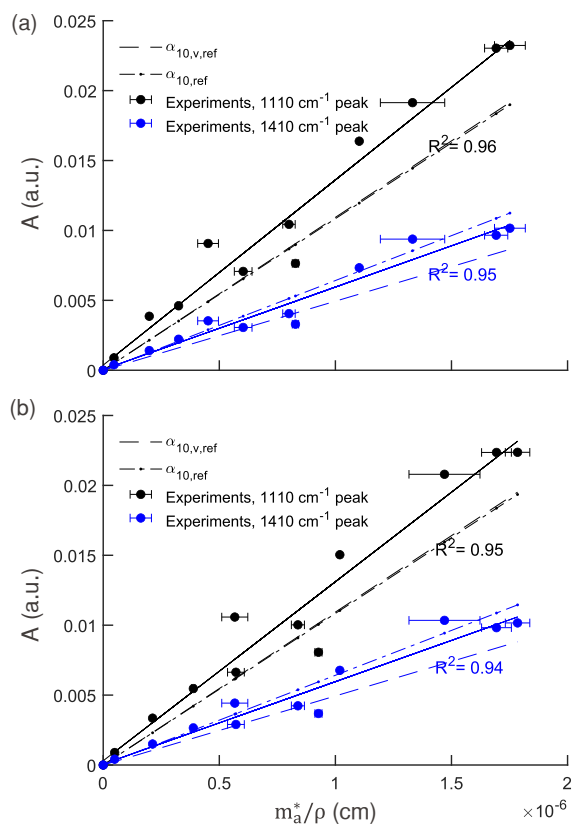
Figure S6. (a) Response of IR absorbance (A) against the equivalent thickness (cm) calculated assuming $\phi_R(r_b) = 1$ for absorbance at the peak near 1110 cm^{-1} (for $\nu_3(SO_4^{2-})$)) and at the peak near 1410 cm^{-1} (for $\nu_4(NH_4^-)$). (b) Reproduction of Figure 5b ($\phi_R(r_b) \neq 1$) but using the modified peak heights after removing the PDMS absorption profile (i.e. from the $\alpha_{10,v}$ calculated in Figure S5b) .
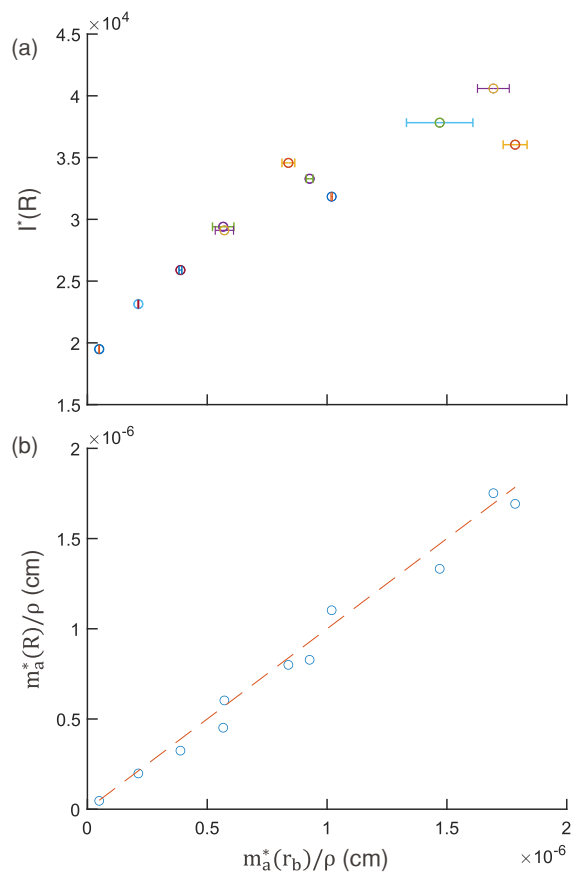
Figure S7. (a) The integrated area under the average intensity curve for each experiment against the volume areal density (same color scheme as Figure 4a). (b) Comparison of the equivalent thickness (cm) calculated from areal mass density on the substrate and that under the beam. The 1:1 line corresponds to the case where $\phi_R(r_b) \equiv 1$.

S4 Estimation of particle absorbance

In the single scattering approximation, the transmittance through an ensemble of particles T_p is related to its optical depth τ. τ is typically written as a product of volumetric number concentration N through path length ℓ and attenuation cross section C_{ext} summed across particles of size i; which can be rewritten in terms of areal number density $N_a = N\ell$ and volume attenuation coefficient $\alpha_v = C_{\text{ext},i}/V_{p,i}$:

$$T_p = e^{\tau}, \text{ where } \tau = \sum_i N_i C_{\text{ext},i}\ell = \sum_i N_{a,i} V_{p,i}\alpha_{v,i} . \tag{S1}$$

$\sum_i N_{a,i} V_{p,i}$ is the total areal volume density or deposition thickness of the equivalent mass in the form of the pure substance. This quantity is equivalent to the product of total areal number density $N_a = \sum_i N_{a,i}$ and the mean particle volume $\overline{V}_p$, and is related to the areal mass density m_a^* and pure substance mass density ρ as presented in the main text:

$$\sum_i N_{a,i} V_{p,i} = N_a \overline{V}_p = \frac{m_a^*}{\rho} . \tag{S2}$$

In the Rayleigh regime: i) absorption dominates the attentuation ($C_{\text{ext},i} \sim C_{\text{abs},i}$), and ii) the volume attentuation coefficient can be written to be independent of size ($\alpha_{v,i} \sim \alpha_v$) (Bohren and Huffman, 1983). Therefore, the decadic absorbance is

$$A_p = -\log_{10} T_p = \frac{\tau}{\ln 10} = \frac{\alpha_v}{\ln 10}\frac{m_a^*}{\rho} . \tag{S3}$$

$\alpha_v/(\rho\ln 10)$ is the decadic mass attenuation coefficient. For further simplification in notation, the volume attenuation coefficient has been written in its decadic form $\alpha_{10,v} = \alpha_v/\ln 10$ for Eq. 2.

The particles are measured on an IR transparent crystal, so the apparent transmittance is T is due to the presence of both particles and the crystal in the path of the beam. In the Rayleigh regime, particle scattering is weak and therefore we neglect multiple scattering (Haenel, 1987; Petzold and Schönlinner, 2004) and near-field interactions(e.g., Quinten, 2011) between the particle layer and the crystal. In this approximation, the transmittance through the particles (T_p) and crystal (T_c) are considered to be independent. (T_c is related to its reflectance by $1 - R_w$, which can be derived from Fresnel equations.) Letting I equal the single beam spectrum through the sample, I_w the single beam spectrum through the clean crystal, and I_0 the single beam spectrum of the empty chamber (conventional background), T_p can be obtained by normalizing the sample spectrum I by the clean crystal T_c spectrum, as often done for spectroscopic measurement of solutions in liquid cells:

$$T = \frac{I}{I_0} = T_p T_c, \ T_c = \frac{I_w}{I_0}, \text{ and } T_p = \frac{T}{T_c} = \frac{I}{I_w} . \tag{S4}$$

However, an assumption in this strategy is that I and I_c are measured under similar conditions. An additional consideration for this analysis is that particles are collected on the crystal for a finite period of time, during which changes in the conditions (source strength, detector efficiency) under which the two spectra are acquired may change (Scanlon et al., 1979). In contrast to single beam spectra, transmittance measurements are approximately time-invariant if the background through the empty chamber is taken close in time (i.e., close in environmental conditions):

$$T_c = \frac{I_w(t)}{I_0(t)} \approx \frac{I_w(t')}{I_0(t')} . \tag{S5}$$

Therefore, the particle contribution to transmittance is obtained from transmittances of the sample and clean crystal (each referenced to empty chamber backgrounds taken close in time). This operation amounts to blank subtraction in terms of absorbances (Eq. 2).

S5 Deposited particle distribution

The areal mass density within an arbitrary radius r is related to the deposited size and spatial distribution of particles, which is unmeasured. Therefore, we describe how this quantity is related to the collected particle size distribution and number concentrations obtained from aerosol flow system measurements, and adjustment factor obtained from scattered light intensity from an optical microscope.

We consider that the the areal number concentration of deposited particles N_a is dependent on size and radial position on the crystal. Given mass density of substance (ρ), the mass deposited over unit area (m_a) and integrated areal mass density (m_a^*) within radius r are given from the deposited volume size distribution:

$$m_a(r) = \rho \frac{\pi}{6} \int_{D_{\mathrm{p,min}}}^{D_{\mathrm{p,max}}} D_{\mathrm{p}}^3 \frac{\partial N_a(r, \ln D_{\mathrm{p}})}{\partial \ln D_{\mathrm{p}}} d\ln D_{\mathrm{p}} \tag{S6}$$

$$m_a^*(r) = \frac{2}{r^2} \int_0^r r' m_a(r') dr' \ . \tag{S7}$$

The number size distribution of deposited particles integrated over the entire crystal is determined by the collection efficiency η and volumetric number size distribution $N^\#$ of particles that entered the collector (together with the flowrate and collection time):

$$2\pi \int_0^R r' \frac{\partial N_a(r, \ln D_{\mathrm{p}})}{\partial \ln D_{\mathrm{p}}} dr' = \frac{d(\eta(\ln D_{\mathrm{p}}) N^\#(\ln D_{\mathrm{p}}))}{d \ln D_{\mathrm{p}}} Qt \ . \tag{S8}$$

From Eqs. S6–S8, the average areal mass density over the entire crystal is

$$m_a^*(R) = \frac{Qt\rho}{6R^2} \int_{D_{\mathrm{p,min}}}^{D_{\mathrm{p,max}}} D_p^3 \frac{d(\eta(\ln D_{\mathrm{p}}) N^\#(\ln D_{\mathrm{p}}))}{d \ln D_{\mathrm{p}}} d\ln D_{\mathrm{p}} \ . \tag{S9}$$

Having estimated the total number concentrations at a different time resolution than the size distribution in our experiments, we estimate $m_a^*(R)$ from eq. 3, which is mathematically equivalent to eq. S9.

The scattered intensity is interpreted as being proportional to the mass loading of particles. Therefore, the measured positional intensity I for a ring at r (integrated over all angles) can be related to m_a, and the intensity I^* integrated over r related

to m_a^*:

$$I(r) \propto 2\pi \int_r^{r+\Delta r} r' m_{\mathrm{a}}(r')dr' \tag{S10}$$

$$I^*(r) = \int_0^r \frac{dI(r')}{dr'}dr' \propto \pi r^2 m_{\mathrm{a}}^*(r) \ . \tag{S11}$$

The areal mass density ratio is estimated from the integrated beam intensities at two radii r and r':

$$\phi_r(r') = \frac{m_a^*(r')}{m_a^*(r)} = \frac{I^*(r')/r'^2}{I^*(r)/r^2} \ . \tag{S12}$$

For visualization of the radial profile, the positional intensities are normalized by the ring area, which grows with r:

$$\bar{I}(r) = \frac{I(r)}{2\pi \int_r^{r+\Delta r} r'dr'} \ . \tag{S13}$$

S6 Limit of detection

The signal-to-noise (SNR) ratio is characterized by the ratio of mean to noise levels. In decible (dB) units (Northrop, 2011):

$$SNR = 20\log_{10}\frac{A_{\mathrm{peak}}}{A_{\mathrm{noise}}} \ . \tag{S14}$$

A_{peak} is the signal value of the peak height at 1410 cm^{-1}, which we estimate from the maximum of a LOESS (locally estimated scatterplot smoothing) curve fitted to each peak (using a 10% span for smoothing). A_{noise} is the signal noise value, which we estimate as the standard deviation of residuals obtained from subtracting a LOESS curve fitted to the original signal in a region free from major bands, between 2150–2080 cm^{-1} (using a 4% span for smoothing). A region separate from the peak is used to estimate the noise since subtraction of the LOESS curve from the spectrum at the 1410 cm^{-1} peak leaves residuals that inflate the A_{noise} estimate, and we do not expect the noise level to be wavenumber-specific (Milosevic, 2012). Spectra from all measurements, including VAIRS, is used to examine the wide range of SNRs encountered in our experiments.

SNR increases with $m_{\mathrm{a}}^*(r_{\mathrm{b}})$ with a different relation for each aperture size due to differences in the level of A_{noise} (Figure S8). Three standard deviations (limit of detection, or LOD) and ten standard deviations (limit of quantification, or LOQ) of the noise correspond to 9.5 and 20 dB, respectively. While the 1410 cm^{-1} peak is detectable in the lowest SNR (9.9 dB) spectrum (not shown), a more useful spectrum in which even the diffuse peak of the N-H stretch at 3210 cm^{-1} emerges around 20 dB. Features in the spectrum are even more clearly visible at the 30 dB level, which is typically considered to be a "high SNR" value (Villares et al., 2014). 9.5, 20, and 30 dB correspond to $m_{\mathrm{a}}^*(r_{\mathrm{b}}) = 3$ ng/cm^2, 12 ng/cm^2, 44 ng/cm^2, respectively, for the aperture size of 6 mm. Assuming $\phi_{\mathrm{R}}(r_{\mathrm{b}}) \approx 1$, the LOQ (20 dB threshold) in terms of absolute mass for the 2.54 cm optical crystal is $m^* = 68$ ng. While not directly comparable, LOD (9.5 dB) for transmission analysis through PTFE filters reported by Russell et al. (2009) (from standard deviation in integrated absorbance) and Debus et al. (2021) (from standard deviation in predicted blank concentrations) for organic acids or the sulfate ion are typically greater than 300 ng/cm^2, suggesting that collection on ZnSe crystals are at least an order of magnitude more sensitive to the collected mass.
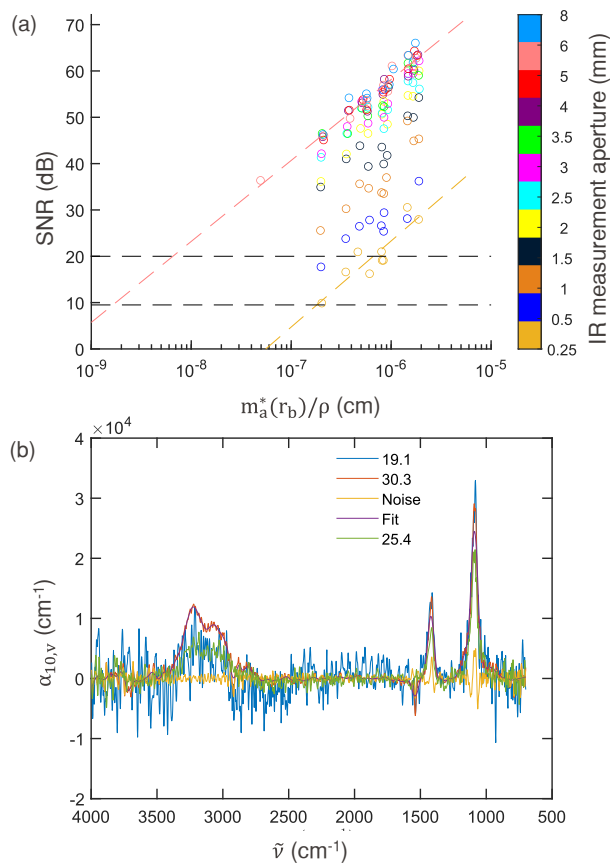
Figure S8. (a) Signal-to-noise ratio (SNR) calculated from IR absorbance spectra (119 points in total); aperture sizes result in different beam size (r_b) and different relationship between deposited mass with SNR. Diagonal lines correspond to the equation $SNR = a + 20\log_{10}(m_a^*(r_b)/\rho)$ for two apertures (6 mm - pink, and 0.25 mm - mustard), where the fitted intercept is interpreted to be approximately $a \approx 20\log_{10}(\alpha_{10,v}/A_{noise})$ in accordance with Eq. 2. Horizontal lines correspond to LOD(9.5 dB) and LOQ(20 dB) threshold. (b) Examples of absorbance spectra, loess fitted curve with 4% span (purple), noise profile (yellow) for three different SNR (dB) values (as labeled).

Implications of this sensitivity for detection or quantification of airborne particles are determined from the sampling and collection strategy. The deposited areal mass density under the beam $m_a^*(r_b$ on either medium (optical crystal or PTFE filters) can be expressed as a product of the airborne mass concentration c and effective path length ℓ:

$$m_a^*(r_b) = c\ell, \text{ where } \ell = \phi_R(r_b)\,\eta\,v_f t \text{ and } v_f = \frac{Q}{a_s} . \tag{S15}$$

The effective path length is the product of face velocity v_f and sampling duration t adjusted for collection efficiency η and deposition uniformity $\phi_R(r_b)$. The face velocity is conventionally defined by the flow rate Q and deposit envelope (collection area) on the substrate a_s. These expressions provide a useful relation between the apparent absorbance of deposited particles
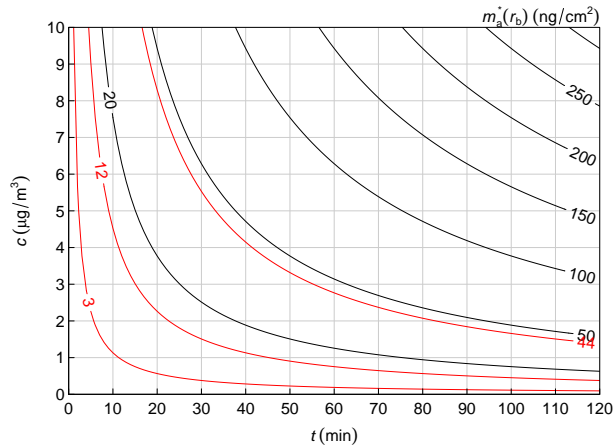
Figure S9. Areal mass densities $m_a^*(r_b)$ in units of ng/cm^2 for a given average airborne concentration c and sampling time t. Red lines indicate values for 9.5, 20, and 30 dB.

(Eq. 2) and airborne concentrations: $A = (\alpha_{10,v}/\rho)c\ell$. However, having calculated the LOQ in terms of $m_a^*(r_b)$ above, Eq. S15 is sufficient for estimating the threshold (Figure S9) in terms of average c for fixed t, or the required t for average c, from the LOQ estimated for $m_a^*(r_b)$ (neglecting additional uncertainties from sampling and collection). For instance, a 30-minute sampling interval would permit analysis at the LOQ (20 dB) if the airborne concentration of ammonium sulfate is on average 1.5 µg/m^3 during this period. Our ESP has a lower effective path length for the same sampling time in comparison with PTFE sampling (Table S1) due to flow rate and collection efficiency considerations, but overall sensitivity toward airborne concentrations is compensated by high sensitivity to deposited mass.

Table S1. Filter face velocities and collection efficiencies. $\phi_R(r_b)$ for all configurations are assumed to be unity.

Configuration	Q	a_s	η	$\eta v_f = \ell/t$
	(L min^{-1})	(cm^2)		(cm s^{-1})
This study	2.1	5.1	0.64	4.4
Russell et al. (2009)[a]	8.35	0.79	1	177
Debus et al. (2021)[b]	22.8	3.53	1	107

[a] An annular mask is used to restrict the deposit envelope to a 1 cm disk on a standard 37 mm PTFE filter, which restricts the maximum allowable flowrate due to high pressure drop but results in higher v_f.

[b] The deposit envelope for a 25 mm diameter PTFE filter used in this work is provided by McDade et al. (2009).

References

Bohren, C. and Huffman, D.: Absorption and Scattering of Light by Small Particles, Wiley Science Series, Wiley, 1983.

de Rooi, J. J. and Eilers, P. H.: Mixture models for baseline estimation, Chemometrics and Intelligent Laboratory Systems, 117, 56–60, https://doi.org/10.1016/j.chemolab.2011.11.001, 2012.

Debus, B., Weakley, A. T., Takahama, S., George, K. M., Schichtel, B., Copleland, S., Wexler, A. S., and Dillner, A. M.: Quantification of major particulate matter species from a single filter type using infrared spectroscopy – Application to a large-scale monitoring network, Atmospheric Measurement Techniques Discussions, 2021, 1–29, https://doi.org/10.5194/amt-2021-382, 2021.

Earle, M. E., Pancescu, R. G., Cosic, B., Zasetsky, A. Y., and Sloan, J. J.: Temperature-Dependent Complex Indices of Refraction for Crystalline (NH4)2SO4, The Journal of Physical Chemistry A, 110, 13 022–13 028, https://doi.org/10.1021/jp064704s, 2006.

Haenel, G.: Radiation budget of the boundary layer. II- Simultaneous measurement of mean solar volume absorption and extinction coefficients of particles, Beiträge zur Physik der Atmosphäre, 60, 241–254, http://scholar.google.com/scholar_lookup?hl=en&volume=60&publication_year=1987&pages=241-247&author=G.+H%C3%A4nel&title=Radiation+budget+of+the+boundary+layer%3A+Part+II%2C+Simultaneous+Measurement+of+Mean+Solar+Volume+Absorption+and+Extinction+Coefficients+of+Particles, 1987.

Kuzmiakova, A., Dillner, A. M., and Takahama, S.: An automated baseline correction protocol for infrared spectra of atmospheric aerosols collected on polytetrafluoroethylene (Teflon) filters, Atmospheric Measurement Techniques, 9, 2615–2631, https://doi.org/10.5194/amt-9-2615-2016, 2016.

Liland, K. H., AlmÃy, T., and Mevik, B.-H.: Optimal Choice of Baseline Correction for Multivariate Calibration of Spectra, Applied Spectroscopy, 64, 1007–1016, https://www.osapublishing.org/as/abstract.cfm?uri=as-64-9-1007, 2010.

McDade, C. E., Dillner, A. M., and Indresand, H.: Particulate Matter Sample Deposit Geometry and Effective Filter Face Velocities, Journal of the Air & Waste Management Association, 59, 1045–1048, https://doi.org/10.3155/1047-3289.59.9.1045, 2009.

Milosevic, M.: Internal Reflection and ATR Spectroscopy, Chemical Analysis: A Series of Monographs on Analytical Chemistry and Its Applications, John Wiley & Sons, Inc., 2012.

Myers, T. L., Tonkyn, R. G., Oeck, A. M., Danby, T. O., Loring, J. S., Taubman, M. S., Sharpe, S. W., Birnbaum, J. C., and Johnson, T. J.: online, https://webbook.nist.gov/cgi/cbook.cgi?ID=C63148629&Mask=80#Refs, 2001.

Northrop, R. B.: Signals and Systems Analysis in Biomedical Engineering, CRC Press, Boca Raton, FL, 2nd edn., 2011.

Petzold, A. and Schönlinner, M.: Multi-angle absorption photometry—a new method for the measurement of aerosol light absorption and atmospheric black carbon, Journal of Aerosol Science, 35, 421–441, https://doi.org/10.1016/j.jaerosci.2003.09.005, 2004.

Quinten, M.: Optical Properties of Nanoparticle Systems: Mie and Beyond, Wiley-VCH Verlag & Co. KGaA, Weinheim, 2011.

Russell, L. M., Takahama, S., Liu, S., Hawkins, L. N., Covert, D. S., Quinn, P. K., and Bates, T. S.: Oxygenated fraction and mass of organic aerosol from direct emission and atmospheric processing measured on the R/VRonald Brownduring TEXAQS/GoMACCS 2006, Journal of Geophysical Research, 114, https://doi.org/10.1029/2008jd011275, 2009.

Scanlon, K., Laux, L., and Overend, J.: The Determination of Absolute Infrared Intensities with a Fourier Transform Spectrometer, Applied Spectroscopy, 33, 346–348, https://doi.org/10.1366/0003702794925552, 1979.

Villares, G., Hugi, A., Blaser, S., and Faist, J.: Dual-comb spectroscopy based on quantum-cascade-laser frequency combs, Nature Communications, 5, https://doi.org/10.1038/ncomms6192, 2014.